

This is a postprint version of the following published document:

Tajmar, M., & Sánchez-Arriaga, G. (2021). A bare-photovoltaic tether for consumable-less and autonomous space propulsion and power generation. *Acta Astronautica*, 180, 350-360.

DOI: <https://doi.org/10.1016/j.actaastro.2020.12.053>

© 2021 IAA. Published by Elsevier Ltd. All rights reserved.



This work is licensed under a [Creative Commons Attribution-NonCommercial-NoDerivatives 4.0 International License](https://creativecommons.org/licenses/by-nc-nd/4.0/).

# A bare-photovoltaic tether for consumable-less and autonomous space propulsion and power generation

M. Tajmar<sup>1</sup> and G. Sánchez-Arriaga<sup>2</sup>

<sup>1</sup>Institute of Aerospace Engineering, Technische Universität Dresden, Marschnerstr. 32,  
01307 Dresden, Germany

<sup>2</sup>Bioengineering and Aerospace Engineering Department, Universidad Carlos III de  
Madrid, Leganés, Madrid, 28911, Spain

## Abstract

State-of-the-art electrodynamic tethers reach a steady electric current by using a bare segment to capture electrons passively from the ambient plasma (anodic contact) and an active electron emitter or a tether segment coated with a low-work-function material (cathodic contact) to emit electrons back and close the electrical circuit. This work proposes to take advantage of recent developments on thin-film solar cells and insert a photovoltaic (pv) tether segment in between the anodic and the cathodic contacts. Since thin-film solar cells can be folded and manufactured with any desired length and the same cross-section dimensions as the bare segment, i.e. width and thickness around few centimeters and tens of microns, the resulting device is compact and preserves bare tether simplicity. Detailed analysis of the current and voltage profiles throughout the tether shows that the electrical power introduced by the pv-segment into the tether-plasma circuit improves the performance and makes them less dependent on ambient conditions. The pv-segment decreases considerably the tether-to-plasma bias at the cathodic contact, thus opening the possibility to emit substantial current while using consumable-less electrons emitters like thermionic and electron field

emitters. The pv-segment also favors the current collection by increasing the tether-to-plasma bias at the bare segment. Propulsion and power generation applications and alternative architectures of bare-pv tethers are briefly discussed.

## Nomenclature

$A_t$	=	tether cross-sectional area, $m^2$
$\mathbf{B}$	=	ambient magnetic field, $T$
$\mathbf{E}$	=	motional electric field, $V/m$
$E_m$	=	motional electric field component along the tether, $V/m$
$e$	=	elementary charge, $C$
$E_{cell}$	=	cell efficiency
$f$	=	illumination factor
$\mathbf{F}_L$	=	Lorentz force, $N$
$h_t$	=	tether thickness, $m$
$I$	=	tether current, $A$
$i_{av}$	=	normalized average current
$I_*$	=	bare tether short-circuit current, $A$
$I_{sc}$	=	short-circuit current of a cell, $A$
$I_d$	=	dark saturation current of a diode, $A$
$k_B$	=	Boltzmann constant, $m^2kg/s^2K$
$L_t$	=	total tether length, $m$
$L_b$	=	bare segment length, $m$
$L_{pv}$	=	pv segment length, $m$
$L_*$	=	bare tether characteristic length, $m$
$m_e$	=	electron mass, $kg$
$N_0$	=	ambient plasma density, $1/m^3$
$p_t$	=	tether perimeter, $m$

$T_{pv}$	=	pv segment temperature, $K$
$T_t$	=	tether temperature, $K$
$\mathbf{u}_t$	=	unit vector along the straight tether
$\mathbf{v}$	=	spacecraft velocity, $m/s$
$V_*$	=	bare tether characteristic voltage, $V$
$V_t$	=	tether bias, $V$
$V_p$	=	plasma bias, $V$
$V_{pv}$	=	voltage across a pv cell, $V$
$V_{oc}$	=	open-circuit voltage of a cell, $V$
$V_T$	=	thermal voltage, $V$
$V_k$	=	knee voltage of bypass diode, $V$
$V_C$	=	potential drop of the electron emitter, $V$
$W_t$	=	coated tether work function, $eV$
$w_t$	=	tether width, $m$
$x$	=	distance along the tether from the anodic point, $m$
$\eta_{cell}$	=	delivered-to-maximum power ratio
$\sigma_t$	=	tether conductivity, $1/\Omega m$

## 1 Introduction

Since 1965, when Drell et al proposed the use of conductors to drag and propel satellites in the ionosphere [1], electrodynamic tethers pursued the old dream of developing a consumable-less and simple system to generate in-orbit power and thrust. The insulated

tether with active plasma contactors at both ends envisaged by Moore [2] one year later, which was successfully demonstrated in the Plasma Motor Generator mission [3], was considerably simplified by the bare tether concept in 1993 [4]. A bare tether captures electrons passively, thus eliminating the need for an active anodic plasma contactor. In order to eliminate the active cathodic plasma contactor, it has been recently proposed to coat a tether segment with a low-work-function (low-W) material and use the passive thermionic [5] and photoelectric [6] effects to close the circuit. This important progress has been strengthened with key advances on tether dynamics and control [7, 8, 9, 10, 11] and the crucial change of moving from the old circular cross-section (wire) to the current tape-like configuration, which improves tether performance [12], increases tether survivability [13, 14, 15] and strongly mitigates the risk identified in past work for round tethers [16].

During the last few decades, electrodynamic tethers followed a path towards simplicity and reliability, but the practical implementation of a fully consumable-less system still presents some difficulties due to the cathodic contact. Regarding low-W tethers (LWT), and albeit it is currently an active field of research [17], a coating with low enough work function has not been developed yet. In the case of bare tethers equipped with electron emitters, there is a dilemma. For high current applications, for instance above 0.5 amps, the favorite emitter may be a hollow cathode because it requires low power [18]. However, since hollow cathodes need expellant, they increase the complexity of the tether system and limit the mission duration. For low current applications, there exist fully consumable-less devices (thermionic and electron field emitters), but they typically need much more power due to space-charge effects. This problem disappears if the tether system is on-board a spacecraft that could provide power. However, electrodynamic tether applications, including deorbiting satellites [19] at the end-of-life, orbital re-boost [20], mega-constellations maintenance [21], and orbital station-keeping [22], among others, would benefit if a fully autonomous tether device is developed.

We propose here to combine thin-film solar cell technology with the bare tether con-

cept to construct a compact and fully consumable-less tether system. Photovoltaic cells transform solar energy into electrical energy and can reach an efficiency of around 30% [23]. If adequately connected into the tether-plasma electric circuit, the power delivered by the cells can improve the performance and make feasible the use of consumable-less emitters that would not be compatible with a standard bare tether due to the lack of available power. In order to keep a low complexity and develop a compact system, the proposed concept takes advantage from the fact that the dimensions of the cross-section of the photovoltaic (pv) cell can match the dimensions of a standard bare tether, i.e. width and thickness around few centimeters and several tens of microns, respectively. In addition, thin-film pv cells are so flexible that they can be coiled up just like a normal tether. Since any length can be reached by stacking the cells, a pv tether segment can be manufactured and connected between the bare tether and the cathodic contactor. As compared with standard configurations, an interesting amount of power is obtained while barely impacting on system complexity. The pv-segment can be rolled up down to a diameter of around 10 cm in a deployment mechanism together with the bare segment.

This work is organized as follows. Section 2 presents the mechanical and electrical architecture of a bare-pv tether and summarizes some basic concepts about solar cells. A model for the current and voltage profiles throughout a bare-pv tether equipped with an electron emitter, together with the main figures of merit of the system, are introduced in Sec. 3. Tether performance for a typical deorbiting mission with a bare-pv tether is investigated in Sec. 4. Design considerations and the required modifications in the model to address other tether modes (reboost and power generation) and types (LWT) are discussed in Secs. Sec. 5.1 and 5.2, respectively. The conclusions are summarized in Sec. 6.

## 2 System architecture

There are several possible mechanical and electrical architectures to combine bare tether and pv technologies. For instance, one may consider a tether that would alternate bare

and pv segments. A tether that captures electrons from one side and has solar cells on the other side is also an interesting alternative. This work proposes a tether system with a photovoltaic segment inserted between a bare segment and the cathodic contactor, which can be an active electron emitter or a tether segment coated with a low-W material. For instance, panel (a) of Fig. 1 shows a pv-segment of length  $L_{pv}$  electrically connected at point  $P$  with a bare segment of length  $L_b$ . The pv-segment is connected at point  $C$  with an active device that emits the electrons at a cost of a potential drop  $V_C < 0$ . Panel (b) shows a similar configuration, but the electron emitter is substituted by a tether segment of length  $L_c$  coated with a material of work function  $W_t$ . In either case, the pv-segment is made of a set of  $N_{cell}$  solar cells connected in series. We enumerate them from 1 to  $N_{cell}$  and starting from the cell that is the closest to the cathodic end. The negative pole of the first cell is connected to the cathodic contactor, i.e. at points C and S for the configurations in panels (a) and (b), and the positive pole of the last cell is connected to the bare segment at point  $P$ .

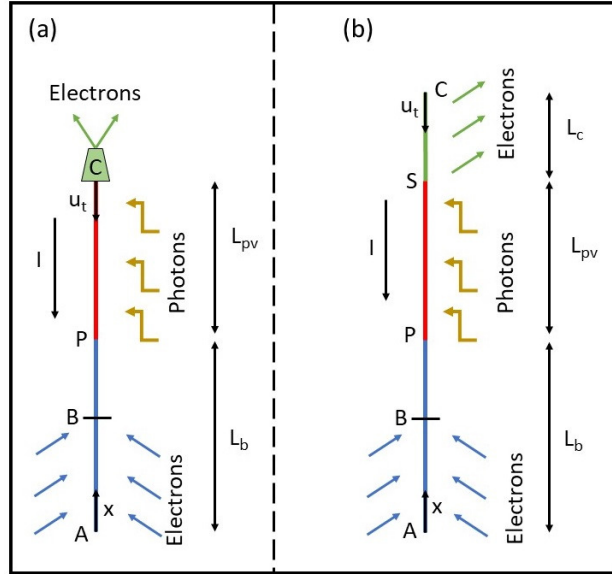


Figure 1: Bare-pv tether with an electron emitter (a) and a segment coated with a low-W material (b). Point B is the zero-bias point.



Panel (a) in Fig. 2 shows a detail of the pv segment. One face is prepared to receive the Sun illumination and the other is designed to radiate the heat. Each cell has silver connectors on one end that connect to the next cell and a bypass diode to avoid a reduction in power if one element fails or is in shadow. It is also possible to put a bypass diode in parallel, but in opposite polarity, with a group cells to reduce cost and complexity. All the tether segments have a tape-like cross sections. For simplicity, we assume that the width ( $w_t$ ) and the thickness ( $h_t$ ) of the cross-section is the same throughout the tether. The analysis also uses the perimeter  $p_t \approx 2w_t$ , the cross-sectional area  $A_t = w_th_t$ , the conductivity of the bare segment  $\sigma_t$ , and the total tether length  $L_t = L_b + L_{pv}$  or  $L_t = L_b + L_{pv} + L_c$ . For later use, we also introduce the unit vector  $\mathbf{u}_t$  along the assumed straight tether and pointing from point  $C$  to  $A$ . The electric current carried by the tether reads  $\mathbf{I} = I(x)\mathbf{u}_t$ , where we called  $x$  to the coordinate measured from the anodic tip  $A$ .

Panel (b) of Fig. 2 shows the equivalent electric model of the solar cells in our work. Every solar cell is substituted by a current generator in parallel with an ideal diode. In order to avoid hot-spot heating and mitigate performance losses when a cell is shadowed, bypass diodes connected in parallel but with opposite polarity are added. These diodes (pink elements in Fig. 2) act as open circuits in normal operation because they are reverse biased. In case a cell is reverse biased due to a mismatch in the current, then the bypass diode conducts and the potential drop in the poor cell (for instance because it is shadowed) is limited to a single diode potential drop. The electric current  $I_j$  circulating through the cells are then given by [24]

$$I_j(\Delta V_j) = I_{sc} \left[ 1 - \frac{e^{\Delta V_j/V_T} - 1}{e^{V_{oc}/V_T} - 1} \right] + I_d \left( e^{-\frac{\Delta V_j}{V_T}} - 1 \right), \quad j = 1 \cdots N_{cell} \quad (1)$$

where  $\Delta V_j = V_{t,j+1} - V_{t,j}$  is the bias difference between the poles of the cell with number  $j$ . We added the subscript  $t$  to emphasize that it is a tether bias and distinguish them from bias with subscript  $p$ , which denotes potential at the faraway plasma (see below). The first term represents the current of the cell, where  $I_{sc}$  is the short circuit current,  $V_{oc}$  the open

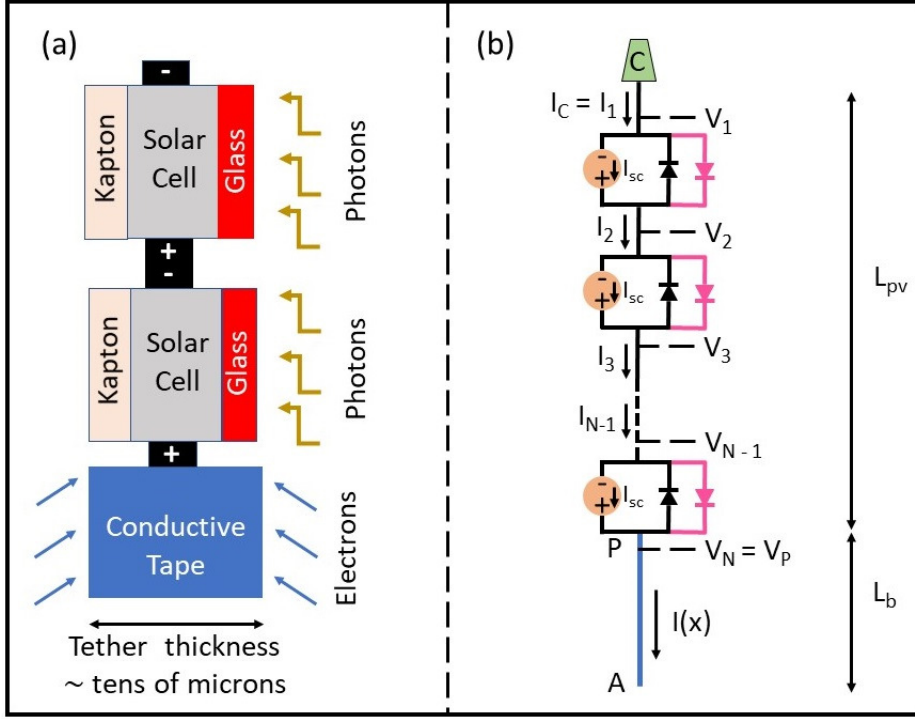


Figure 2: Panel (a) shows a detail of the solar cells and panel (b) the equivalent circuit of the cells used in this work.

circuit voltage,  $V_T = k_B T_{pv} / e$  the thermal voltage,  $T_{pv}$  the temperature of the cell,  $k_B$  the Boltzmann constant, and  $e$  the elementary charge. Series and shunt resistances, which can be incorporated in more elaborated models, are here ignored for simplicity. The second term in Eq. (1) is the current of the bypass diode and  $I_d$  its dark saturation current. If forward biased and illuminated, the cell transforms the power received from the Sun ( $W_{sun}$ ) into electric power ( $W_{e,j} = I_j \Delta V_j$ ) with an efficiency  $E_{cell} = W_e / W_{sun}$ . The maximum delivered power is reached at the Maximum Power Point ( $\Delta V_{j,MPP}$  and  $I_{j,MPP}$ ), which is found from the condition  $dW_{e,j} / d\Delta V_j = 0$ . If the cell is not illuminated, the current flows through the bypass diode at a cost of a potential drop  $V_k < 0$  (knee voltage). We define

here the knee voltage as the reverse voltage to reach a current of 100 mA

$$\tilde{V}_k \equiv \frac{V_k}{V_T} \approx -\ln \left( 1 + \frac{0.1A}{I_d} \right) \quad (2)$$

The current-voltage characteristic given by Eq. (1) is shown in Fig. 3 for illuminated cells with and without a bypass diode, and for a non-illuminated ( $I_{sc} = 0$ ) cell with a bypass diode. Key points, voltages, and currents, like the MPP (red cross),  $V_{oc}$ ,  $V_k$ , and  $I_{sc}$ , are shown.

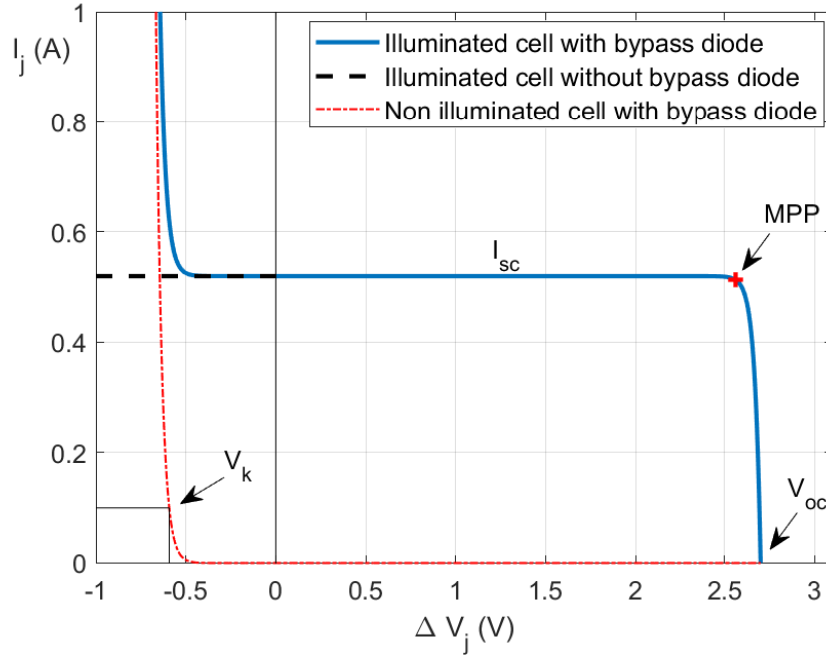


Figure 3:  $I_j - \Delta V_j$  characteristic curve of a solar cell with and without a bypass diode. The Maximum Power Point (MPP) and the knee voltage given by Eq. 2 are also shown.

Before presenting a detailed model of the tether system in Sec. 3, we make here some simple estimations to get a physical and engineering insight of the concept. Consider a pv segment with  $w_t = 2.5cm$  and  $L_{pv} = 100m$  (area equal to  $2.5 m^2$ ) and the typical values of space thin film solar cells in Table 1 [23]. For the same cell area of the one in Table 1, the length of each cell is  $L_{cell} = A_{cell}/w_t = 12.4cm$  and the total number of cells is around

$N_{cell} \approx 800$ . The total power delivered by the pv segment is estimated as

$$W_{e,pv} = \frac{w_t L_{pv}}{\pi} E_{cell} S_{Sun}, \quad (3)$$

where  $S_{Sun} = 1366 W/m^2$  is the solar constant and the factor  $1/\pi$  represents the random average orientation of the solar rays with respect to the tape, which only produces power if illuminated on one of its faces. Equation (3) gives a power  $W_e \approx 272 W$  and, if the cells operate at a voltage close to  $V_{oc}$  and we assume that only half of them are illuminated, the bias between the ends of the pv segment is around  $800 \times 2.7V/2 \approx 1kV$ . Such estimations for the power and the bias highlight the high potential of the combination of bare and pv technologies. However, as shown below, a detailed analysis of the current and voltage profiles is necessary to make a good design of the system and reach high performance.

Variable	Symbol	Value
Efficiency	$E_{cell}$	0.25
Area	$A_{cell}$	$31cm^2$
Open circuit voltage	$V_{oc}$	2.7V
Short circuit current	$I_{sc}$	0.52A
Cell temperature	$T_{pv}$	100 °C
Dark saturation current	$I_d$	$10^{-9} A$

Table 1: Typical parameters of space thin film solar cells and the bypass diode.

### 3 Current and voltage profiles

The tether system presented in the previous section is attached at point  $A$  or  $C$  to a spacecraft of mass  $M_s$ , which orbits at velocity  $\mathbf{v}$  and in the presence of the planet's magnetic field  $\mathbf{B}$ . Due to the tether system-to-plasma relative velocity  $\mathbf{v}_{rel} \approx \mathbf{v}$ , a motional electric field  $\mathbf{E} = \mathbf{v} \times \mathbf{B}$  appears at the faraway plasma in the tether reference frame. The

plasma potential  $V_p$  is governed by

$$\frac{dV_p}{dx} = E_m \quad (4)$$

Our analysis is restricted to the case  $E_m \equiv (\mathbf{v} \times \mathbf{B}) \cdot \mathbf{u}_t > 0$ , where  $\mathbf{E} \cdot \mathbf{I} > 0$ . In this case, the electromotive force of the pv segment works collaboratively with  $\mathbf{E}$  to drive the current  $\mathbf{I}(x)$ . This is normally called the passive tether mode in the literature because, even in the absence of the pv-segment, the motional electric field would drive the current in the tether. Its working principle is similar to the passive Lorentz drag appearing in a magnet falling inside a pipe of copper. In the case of a tether in active mode ( $E_m \equiv (\mathbf{v} \times \mathbf{B}) \cdot \mathbf{u}_t < 0$ ), exactly the same tether architecture presented in Sec. 2 is valid, but the power supplied by the cells should be large enough to polarize the bare segment positively and the cells act against the motional electric field with  $\mathbf{E} \cdot \mathbf{I} < 0$ . In either case, one of the key figures of merit is the Lorentz force

$$\mathbf{F}_L = \int_0^{L_t} \mathbf{I} \times \mathbf{B} dx \approx (\mathbf{u}_t \times \mathbf{B}) \int_0^{L_t} I(x) dx, \quad (5)$$

The computation of the current profile  $I(x)$  in Eq. (5) requires a detailed analysis of the tether system. Although this work uses some results and methods based on standard bare tether analysis (find more details in Ref. [4] and [25]), the pv segment introduces some important and interesting differences. As usual in bare tether analysis, we introduce the dimensionless variables

$$i(\xi) = \frac{I(x)}{I_*}, \quad \phi(\xi) = \frac{V(x)}{V_*}, \quad \xi \equiv \frac{x}{L_*} \quad (6)$$

with  $I_* \equiv \sigma_t E_m A_t$  the short circuit current of the bare tether,  $V_* \equiv E_m L_*$ ,  $V \equiv V_t - V_p$  the tether-to-plasma bias and

$$L_* \equiv h_t^{2/3} \left( \frac{9\pi^2 m_e \sigma_t^2 E_m}{128 e^3 N_0^2} \right)^{1/3}, \quad (7)$$

the characteristic length gauging ohmic effects [4]. In Eq. (7),  $m_e$  and  $N_0$  are the electron mass and the unperturbed plasma density. As shown below, for a tether system with

an active electron emitter (panel (a) in Fig. 1), the model depends on the following dimensionless parameters

$$\begin{aligned} \xi_b = \frac{L_b}{L_*}, \quad \xi_{pv} = \frac{L_{pv}}{L_*}, \quad \phi_C \equiv \frac{V_C}{V_*}, \quad \lambda \equiv \frac{E_m L_*}{V_T} \\ N_{cell}, \quad i_{sc} = \frac{I_{sc}}{I_*}, \quad \tilde{V}_{oc} \equiv \frac{V_{oc}}{V_T}, \quad i_d = \frac{I_d}{I_*} \end{aligned} \quad (8)$$

Given  $\lambda$  and  $i_d$ , the normalized knee voltage ( $\tilde{V}_k = V_k/V_T$ ) is found from Eq. (2). For clarity, we present in Fig. 4 a scheme of the voltage and current profiles in a bare-pv tether with three cells and only two of them are illuminated. It shows two different cases for the potential profiles: (i)  $E_m(L_b + L_{pv}) > -V_c$  and the pv segment just improves the performance of the system (left), and (ii)  $E_m(L_b + L_{pv}) < -V_c$  and the pv-segment is crucial (middle). In both cases, the current profile is similar (right). Note that, as shown by Eq. (4), the plasma potential varies linearly with the  $x$  coordinate. A detailed justification of potential and current profiles is provided in the next sections.

### 3.1 Bare tether segment

The tether potential profile in the bare segment is governed by Ohm's law  $dV_t/dx = I/\sigma_t A_t > 0$ . Consequently, the tether potential increases monotonically with  $x$  in the bare segment (see Fig. 4). Such equation can be combined with Eq. (4) to find the governing law for the tether-to-plasma bias profile,  $V = V_t - V_p$ . In dimensionless form it reads

$$\frac{d\phi}{d\xi} = i - 1 \quad (9)$$

Points in the bare segment having a positive bias ( $\phi > 0$ ) collect electrons. For a not too large tether width [26], the collected current per unit area is well-described by the Orbital-Motion-Limited law for high bias  $J_{OML} = eN_0\sqrt{2eV/m_e}$  [4, 27]. Within such anodic portion, the current is governed by  $dI/dx = p_t \times J_{OML}$ . This law is valid up to a point  $B$  located at a normalized distance  $\xi_B$  from point A satisfying  $\phi(\xi_B) \equiv 0$ . The high bias approximation is not valid around point  $B$ , but this may represent a small effect that

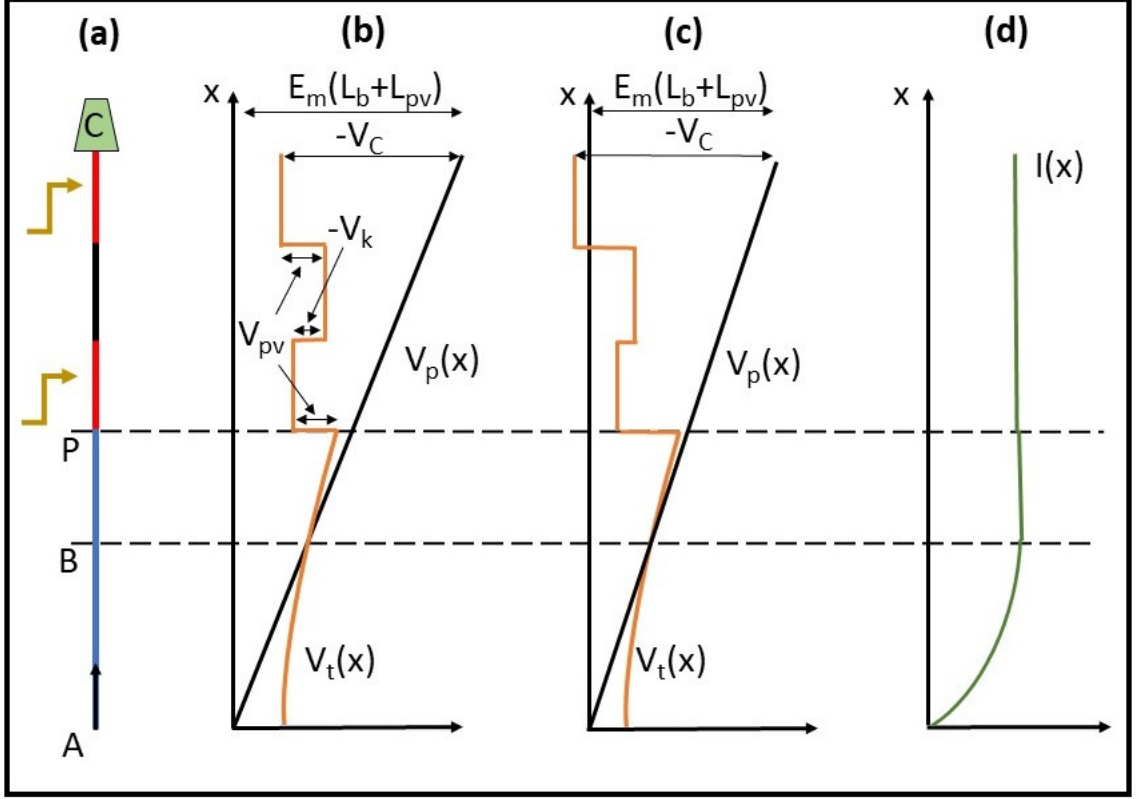


Figure 4: Scheme of a bare-pv tether (a), plasma and tether potential profiles for  $E_m L_t > -V_c$  (b) and  $E_m L_t < -V_c$  (c), and current profile (d).

could be addressed in more refined analysis (see a discussion in Ref. [28]). Depending on ambient and tether parameters, a cathodic segment with  $\phi < 0$  and receiving the impact of ions could develop. Since we have  $m_i/m_e \gg 1$ , with  $m_i$  the ion mass, we can safely take  $dI/dx = 0$  in the cathodic segment. For convenience, we study separately the anodic and the cathodic segments that can be present in the bare portion of the tether. They extend from points A to B and from points B to P in Fig. 1, respectively.

### 3.1.1 The anodic segment

For  $0 \leq \xi \leq \xi_B$ , and using the variables in Eqs. (6), the law  $dI/dx = p_t \times J_{OML}$  reads

$$\frac{di}{d\xi} = \frac{3}{4}\sqrt{\phi} \quad (10)$$

System (9)-(10) admits the first integral [4]

$$(i - 1)^2 = \phi^{3/2} + 1 - \phi_A^{3/2}, \quad (11)$$

where we used that  $i(0) = 0$  and defined  $\phi_A \equiv \phi(0)$ . Equation (10) shows that the current increases monotonically from zero at point  $A$  up to a maximum  $i_B$  at point  $B$  (See Fig. 4). Conventional bare tethers with ohmic effects satisfy  $i_B < 1$  and  $\phi_A < 1$  [4], and the bias decreases monotonically according to Eq. (9). However, a bare-pv tether is different because the pv-segment delivers a power that can produce  $i_B > 1$  and  $\phi_A > 1$ . A detailed analysis of the current and voltage profiles in the bare segment as a function of  $\phi_A$  is then needed to understand the behavior of the solution.

For  $\phi_A = 1$ , the integration of Sys. (9)-(10) with the boundary conditions  $i(0) = 0$  and  $\phi(0) = \phi_A = 1$  is straightforward and gives the profiles

$$\phi(\xi) = \left(1 - \frac{\xi}{4}\right)^4 \quad (12)$$

$$i(\xi) = 1 - \left(1 - \frac{\xi}{4}\right)^3 \quad (13)$$

This solution only holds for  $\xi < 4$ . If  $\xi_b > 4$ , a cathodic segment develops. For  $\phi_A < 1$ , the current increases monotonically but it cannot exceed the short circuit current because orbits can not cross each other in the  $\phi - i$  plane and the solution for  $\phi_A = 1$  satisfies  $i(\xi) \leq 1$ . Following Ref. [25] we do not use variable  $\xi$ , but an auxiliary variable  $v$  to find



the following profiles from Eqs. (9)-(10)

$$\phi(v) = \left(1 - \phi_A^{3/2}\right)^{2/3} \sinh^{4/3} v, \quad (14)$$

$$i(v) = 1 - \sqrt{1 - \phi_A^{3/2}} \cosh v, \quad (15)$$

$$\xi(v) = \frac{4}{3} \left(1 - \phi_A^{3/2}\right)^{1/6} [F_s(v_{c0}) - F_s(v)], \quad (16)$$

where we defined the variable  $\cosh v_{c0} \equiv 1/\sqrt{1 - \phi_A^{3/2}}$  and the function

$$F_s(x) \equiv \int_0^x \sinh^{1/3} \zeta d\zeta \quad (17)$$

Although it may look cumbersome, this parametrization is convenient. Function  $F_s$  can be computed analytically with a series expansion, thus reducing the computational cost of tether dynamic simulations considerably. We also observe that a cathodic segment develops if  $\xi_b > \xi_B \equiv 4(1 - \phi_A^{3/2})^{1/6} F_s(v_{c0})/3$  and  $\xi_B \rightarrow 4$  as  $\phi_A \rightarrow 1$ .

One of the novelties of the bare-pv tether is that solutions with  $\phi_A > 1$  are also possible. An extension of the methodology of Ref. [25] to the analysis of Eqs. (9)-(10) yields

$$\phi(v) = \left(\phi_A^{3/2} - 1\right)^{2/3} \cosh^{4/3} v \quad (18)$$

$$i(v) = 1 + \sqrt{\phi_A^{3/2} - 1} \sinh v \quad (19)$$

$$\xi(v) = \frac{4}{3} \left(\phi_A^{3/2} - 1\right)^{1/6} [F_c(v) - F_c(v_{s0})] \quad (20)$$

where we defined the variable  $\sinh v_{s0} \equiv -1/\sqrt{\phi_A^{3/2} - 1}$  and the function

$$F_c(x) \equiv \int_0^x \cosh^{1/3} \zeta d\zeta \quad (21)$$

In this case the bias is always positive. For any length of the bare tether  $\xi_b$ , no cathodic segment develops because the bias profile exhibits a minimum  $\phi_m \equiv \left(\phi_A^{3/2} - 1\right)^{2/3} > 0$  at  $\xi_m \equiv \xi(v = 0)$ .

The results of the analysis of the anodic segment are summarized in Fig. 5, which shows current and voltage profiles in the  $i - \phi$  plane for several values of  $\phi_A$  and parametrized

by  $\xi$ . For each profile, the value of  $\phi_A$ , which is the potential for  $\xi = 0$ , is the intersection of the line with the vertical axis ( $i = 0$  line). For profiles with  $\phi_A > 1$ , the bias exhibits a minimum if the length is larger than  $\xi_m$ . For profiles with  $\phi_A < 1$ , the potential decreases monotonically. In case the tether length is larger than  $\xi_B$ , a cathodic segment with negative bias and constant current develops. Such a segment is studied in the next section.

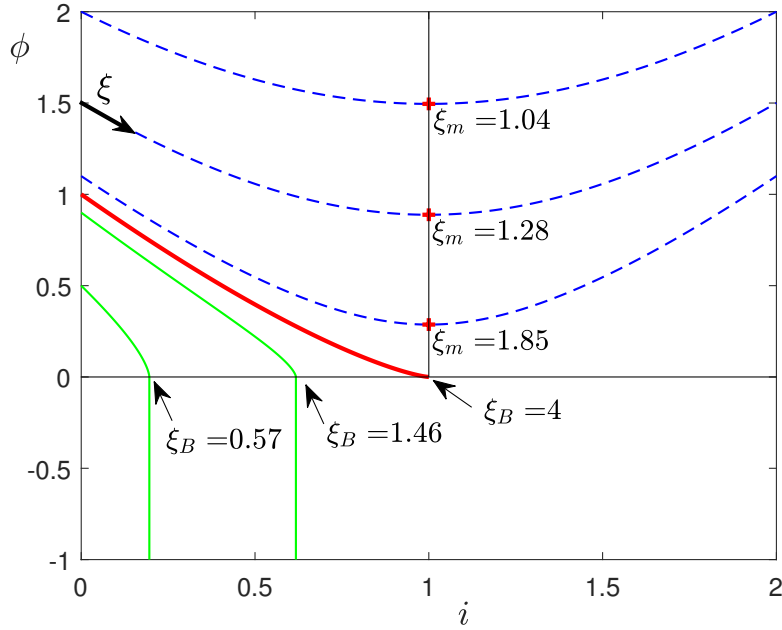


Figure 5: Current and voltage profiles in the bare segment for  $\phi_A = 0.5$  and  $0.9$  (green solid),  $\phi_A = 1$  (thick red line) and  $\phi_A = 1.1, 1.5$  and  $2$  (dashed blue lines). Each curve is parametrized by the variable  $\xi$ , which has value  $\xi = 0$  at the anodic point A ( $i = 0, \phi = \phi_A$ ).

### 3.1.2 Cathodic segment

If  $\xi_b > \xi_B$  and  $\phi_A \leq 1$ , then a cathodic segment develops within the range  $\xi_B \leq \xi \leq \xi_b$ . The integration of Eqs. (9) and  $di/dx = 0$  with the conditions  $i(\xi_B) = i_B$ ,  $\phi(\xi_B) = 0$  gives

$$i(\xi) = i_B \quad (22)$$

$$\phi(\xi) = (i_B - 1)(\xi - \xi_B) \quad (23)$$

### 3.1.3 Current and voltage at point P

The analysis of the bare segment in Secs. 3.1.1 and 3.1.2 allowed to write the current and the voltage at point P ( $\xi = \xi_b$ ) as a function of the bias at point A and the length of the bare segment

$$\phi_P|_{bare} = \phi_P|_{bare}(\phi_A, \xi_b) \quad (24)$$

$$i_P|_{bare} = i_P|_{bare}(\phi_A, \xi_b). \quad (25)$$

If  $\phi_A > 1$ , then  $i_P$  and  $\phi_P$  are obtained by evaluating Eqs. (18)-(19) at  $v = v_b$  with  $v_b$  given by Eq. (20) with  $\xi = \xi_b$ . For  $\phi_A \leq 1$ , the computation of  $i_P$  and  $\phi_P$  depends on the length of the bare segment. If  $\phi_A < 1$  and  $\xi_b \leq \xi_B$ , there is no cathodic segment and  $i_P$  and  $\phi_P$  are found by evaluating Eqs. (14)-(15) at  $v = v_b$  with  $v_b$  given by Eq. (16) with  $\xi = \xi_b$ . For  $\phi_A = 1$  and  $\xi_b \leq 4$ ,  $\phi_P$  and  $i_P$  are given by Eqs. (12)-(13) with  $\xi = \xi_b$ . If  $\phi_A < 1$  and  $\xi_b > \xi_B$ , then there is a cathodic segment and Eqs. (22)-(23) provides  $i_P = i_B$  and  $\phi_P = (i_B - 1)(\xi_b - \xi_B)$ , where  $i_B$  and  $\xi_B$  are found by evaluating (15) and (16) at  $v = 0$ . A similar procedure applies for the case  $\phi_A = 1$  and  $\xi_b > 4$  but one directly has  $\xi_B = 4$  and  $i_B = 1$ .

Given  $\phi_A$  and  $\xi_b$ , the values of  $\phi_P$  and  $i_P$  can also be found graphically from Fig. 5. The bias  $\phi_A$  selects a particular curve in Fig. 5 and, when moving from  $\xi = 0$  to  $\xi = \xi_b$  in the curve, the current and the bias change from  $(i = 0, \phi = \phi_A)$  to  $(i = i_P, \phi = \phi_P)$ . For later use, Fig. (6) shows the contour line of  $\xi_b$  in the  $i_P - \phi_P$  plane. The thick and red

line corresponds to the limit  $\xi_b \rightarrow \infty$ .

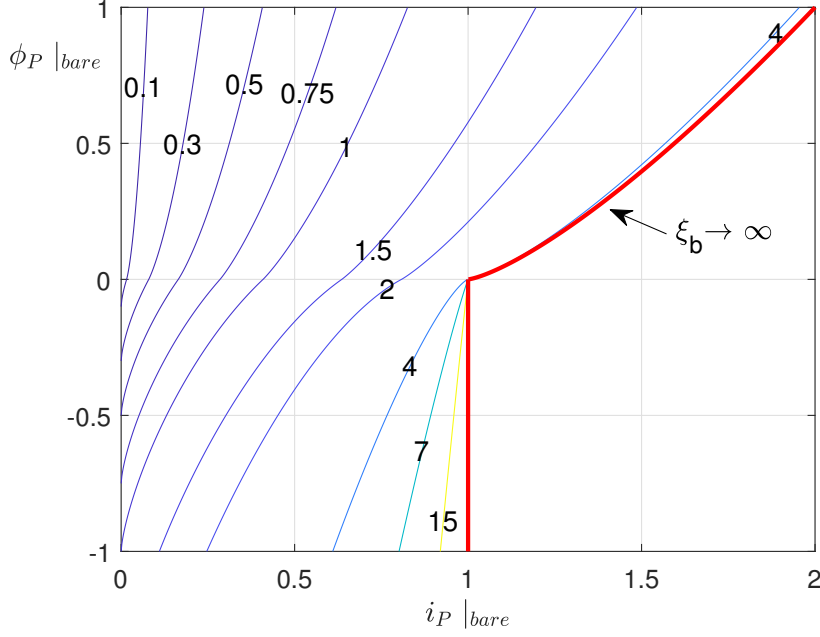


Figure 6: Contour lines of  $\xi_b$  in the  $i_P - \phi_P$  given by the analysis of the bare segment.

### 3.2 Photovoltaic tether segment

Since the solar cells are connected in series and do not exchange current with the ambient plasma, the current at any of them coincides with the current at point P, which is also equal to the one at point C (see Fig. 4). Therefore, we have  $i_C = i_1 = i_2 = \dots = i_{N_{cell}} = i_P$ . Regarding the bias  $\Delta V_j$ , it depends on the illumination conditions and each cell may be different because the tape-tether may be twisted. However, this issue does not preclude to develop a good model. In first place, the detailed values of all the  $\Delta V_j$  are not needed, but just the difference of the tether bias between points P and C in the panel (a) of Fig. 1

$$V_t^P - V_t^C = V_{t,N_{cell}} - V_{t,1} = \sum_{j=1}^{N_{cell}} \Delta V_j \quad (26)$$

In second place, the length of the tether (in the order of a km) is much larger than the length of the cells (tens of cm). Therefore, an average value for the illumination conditions will provide a good value for the difference  $V_t^P - V_t^C$ . For instance, we can assume that only one half of the cells are illuminated and the photogenerated current does not depend on the orientation of the solar rays with respect to the tape, i.e.  $I_{sc}$  is the same for all the illuminated cells. Consequently, the voltage drop at the non-illuminated cells is around  $V_k$  and the voltage difference across the illuminated cells is the same for all of them, say  $V_{pv}$ . We can then approximate Eq. (26) by

$$V_t^P - V_t^C \approx \frac{N_{cell}}{f} (V_{pv} + (f - 1)V_k), \quad (27)$$

where  $f$  is the ratio between the total number of cells and the illuminated cells. This simplified model is illustrated in the scheme of Fig. 4. It considers a pv-segment made of three cells, where the one in the middle is shadowed and the other two are illuminated. The tether bias  $V_t$  changes a value  $V_{pv} > 0$  across each of the two illuminated cells and  $V_k < 0$  at the shadowed cell. Regarding the faraway plasma potential, the integration of Eq. (4) between  $x = L_b$  and  $x = L_b + L_{pv}$  gives  $V_p^C - V_p^P = E_m L_{pv}$ . Using  $V(x) = V_t(x) - V_p(x)$  and after defining  $\tilde{V}_{pv} \equiv V_{pv}/V_T$ , the bias and current at point  $P$  are

$$\phi_P(\tilde{V}_{pv})|_{pv} \equiv \frac{V_t^P - V_p^P}{E_m L_*} = \phi_C + \frac{N_{cell}}{\lambda f} (\tilde{V}_{pv} + (f - 1)\tilde{V}_k) + \xi_{pv} \quad (28)$$

$$i_P(\tilde{V}_{pv})|_{pv} = i_{sc} \left[ 1 - \frac{e^{\tilde{V}_{pv}} - 1}{e^{\tilde{V}_{oc}} - 1} \right] + i_d (e^{-\tilde{V}_{pv}} - 1) \quad (29)$$

with  $i_{sc}$ ,  $\lambda$ ,  $\tilde{V}_{oc}$  and  $i_d$  defined in Eq. (8). The last term in Eq. (29) can be ignored for  $\tilde{V}_{pv} > 0$ . Figure 7 shows Eqs. (28)-(29) in the  $i_P - \phi_P$  plane for some specific values of the parameters and varying  $\xi_{pv}$ . For each curve, which is parametrized by  $\tilde{V}_{pv}$ , the values of  $i_P$  and  $\phi_P$  for  $\tilde{V}_{pv}$  equal to  $\tilde{V}_{oc}$ , MPP, and  $\tilde{V}_k$  are shown.

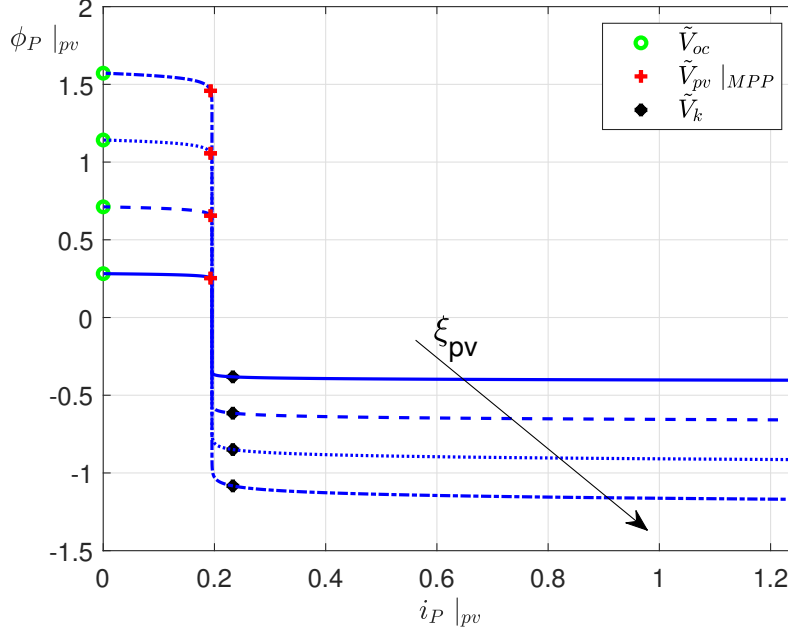


Figure 7: Relation  $i_P - \phi_P$  for several values of  $\xi_{pv}$  obtained from the analysis of the pv segment

### 3.3 Matching of the bare and the pv segments

Given the design parameters in Eq. (8), the two unknowns  $\phi_A$  and  $\tilde{V}_{pv}$  should be found by matching the values of  $\phi_P$  and  $i_P$  given by Eqs. (24), (25), (28) and (29). A graphical and simple procedure consist on combining Figs. 6 and 7, which are very useful to design missions of bare-pv tether in an optimal way. For instance, given the value of  $\xi_b$ , a line is selected in Fig. 6. Once  $\phi_C$ ,  $N_{cell}$ ,  $\lambda$ ,  $\tilde{V}_k$ ,  $\xi_{pv}$ ,  $i_{sc}$ ,  $\tilde{V}_{oc}$  and  $i_d$ , are fixed, a line is chosen in Fig. 7. Both lines intersect at  $(i_P, \phi_P)$ , which also allows to compute  $\phi_A$  and  $\tilde{V}_{pv}$ . Since  $\phi_P|_{bare}$  increases monotonically with  $i_P|_{bare}$ , and  $\phi_P|_{pv}$  decreases monotonically with  $i_P|_{pv}$ , a necessary condition for the occurrence of the intersection is

$$0 < -\phi_C - \frac{N_{cell}}{\lambda f}(f-1)\tilde{V}_k < \xi_b + \xi_{pv} + \frac{N_{cell}}{\lambda f}\tilde{V}_{oc} \quad (30)$$

This constraint implies that the voltage induced by the motional electric field and the illuminated cells should be larger than the sum of the potential drops at the electron emitter and the shadowed cells.

Besides the above graphical procedure, the values of  $\phi_A$  and  $\tilde{V}_{pv}$  can be found numerically with the following algorithm. Starting with an initial guess for  $\tilde{V}_{pv}$ , one first computes  $\phi_P$  and  $i_P$  from Eqs. (28) and (29). The pair  $(\phi_P, i_P)$  defines a point in Fig. 5, which helps to identify whether  $\phi_A$  is larger or smaller than one, and the presence of a cathodic segment. Such a point defines unequivocally a trajectory in the  $i - \phi$  plane together with the value of  $\phi_A$ . It also determines  $\xi_b^{guess}$ , which is the value of  $\xi$  at point  $(\phi_P, i_P)$ . The value of  $\tilde{V}_{pv}$  can be corrected with a Newton-Raphson algorithm until the condition  $\xi_b - \xi_b^{guess} = 0$  is met. Once  $\phi_A$  and  $\tilde{V}_{pv}$  are found, the voltage and current profiles along the tether can be found using the analysis of Secs. 3.1.1, 3.1.2, and 3.2.

### 3.4 Figures of merit

One of the most important figures of merit of the tether system is the normalized average current  $i_{av}$  because it measures tether efficiency [4]. This quantity appears naturally in the computation of the Lorentz force in Eq. (5) and it reads

$$i_{av} = \frac{1}{L_t} \int_0^{L_t} \frac{I(x)}{\sigma_t E_m A_t} dx = \frac{1}{\xi_b + \xi_{pv}} \int_0^{\xi_b + \xi_{pv}} i(\xi) d\xi = \frac{\xi_b + \phi_P - \phi_A + i_P \xi_{pv}}{\xi_b + \xi_{pv}}, \quad (31)$$

where we used that Eq. (9) and the law  $i(\xi) = i_P$  hold in the bare and photovoltaic segments, respectively. For convenience, we construct a second figure of merit for the cells. Taking  $\tilde{V}_{pv} > 0$ , the normalized power delivered by each cell is

$$w_{pv} = \frac{V_{pv} I_P}{V_* I_*} = \frac{\tilde{V}_{pv}}{\lambda} \times i_P \left( \tilde{V}_{pv} \right) \quad (32)$$

and it exhibits a maximum  $w_{MPP}$  at the so-called maximum power point given by the condition  $dw_{pv}/d\tilde{V}_{pv} = 0$ . Such a property suggests to construct a second index defined as

$$\eta_{pv} = \frac{w_{pv}}{w_{MPP}}, \quad (33)$$

which is the ratio of the power delivered by each cell divided by the maximum power that it can deliver.

## 4 Results

This section considers a bare-pv tether with the properties and ambient conditions of Tables 1 and 2. For this particular case, the characteristic variables and the dimensionless parameters are

$$I_* = 2.66A, \quad V_* = 169V, \quad L_* = 1690m, \quad (34)$$

$\lambda \approx 5257$ ,  $i_{sc} \approx 0.2$ ,  $\tilde{V}_{oc} \approx 84$ ,  $i_d \approx 3.76 \times 10^{-10}$ , and  $\tilde{V}_k \approx -18.42$ . For convenience, we study separately in the next three sections the performance of a bare-pv system equipped with electron emitters that have  $V_C = 0$ ,  $-100V$ , and  $V - 1kV$  (ideal, moderate and high potential drops). The impact of the value of the illumination factor  $f$  is also considered.

Symbol	Value	Symbol	Value
$E_m$	0.1 V/m	$N_0$	$10^{11}1/m^3$
$w_t$	1.5 cm	$h_t$	$50\mu m$
$\sigma_t$	$3.54 \times 10^7 1/\Omega m$	$L_{cell}$	$20.7cm$

Table 2: Typical tether and ambient parameters considered in the analysis.

### 4.1 Performance with an ideal electron emitter

Our first example is dedicated to illustrate the design scheme presented in Sec. 3 and the improvement in tether performance by adding a pv segment. For simplicity, we set



$\phi_C = 0$  (ideal electron emitter), consider a short tether with  $\xi_t = 0.2$  (around 340 m for the parameters of Table 2), and set  $f = 2$ . As shown in Fig. 8, the diagrams in the  $i_P - \phi_P$  plane were constructed for three fractions of the pv segment length to total tether lengths ( $L_{pv}/L_t = 0.3, 0.45$  and  $0.6$ ), which are plotted with green, red and black colors. The dashed lines correspond to the  $\phi_P(i_P)$  curves obtained from the analysis of the pv segment by setting  $\xi_{pv} = (0.3, 0.45, 0.6)\xi_t$ . The solid lines were found from the model of the bare segment with  $\xi_b = (0.7, 0.55, 0.4)\xi_t$ . Therefore, the operational point of each tether system, highlighted with a marker, is obtained at the intersection of the solid and dashed lines with the same color. To complement this information, the inset displays the normalized average current  $i_{av}$  versus the ratio  $L_{pv}/L_t$ . As shown by the markers, the three lengths of the pv segment considered previously, i.e. ( $L_{pv}/L_t = 0.3, 0.45$  and  $0.6$ ), are around the point of maximum performance. From the inset we find that a fully bare tether ( $L_{pv}/L_t = 0$ ) has a normalized average current of  $i_{av} \approx 0.028$ ; this value is in agreement with the well-known result for bare tethers with weak ohmic effects,  $i_{av} \approx 0.3\xi_t^{3/2} \approx 0.027$ . For this set of parameters, the optimum is reached when 45% of the tether length is made of pv cells and the maximum average current is  $i_{av} \approx 0.13$ . Consequently, as compared with a pure bare tether with the same total length, the performance of a bare-pv is enhanced a factor of 4.6. Changing from  $f = 2$  to  $f = 3$  (only one third of the cells are illuminated) moves the optimum to  $i_{av} \approx 0.09$ , which is still more than three times the value of a fully bare tether.

## 4.2 Moderate potential drop at the electron emitter

This section studies the impact of the length of the bare-tether when the potential drop of the electron emitter is moderate ( $V_C = -100V$ ), the length of the pv segment is fixed to  $L_{pv} = 50m$ , and the illumination factor is  $f = 2$ . We then have  $\phi_C \approx -0.6$ ,  $\xi_{pv} = 0.03$ , and  $N_{cell} = 242$ . For convenience, we start by revisiting the performance of a fully bare tether with the same total length (see Fig. 9). As shown by the dashed lines in panels

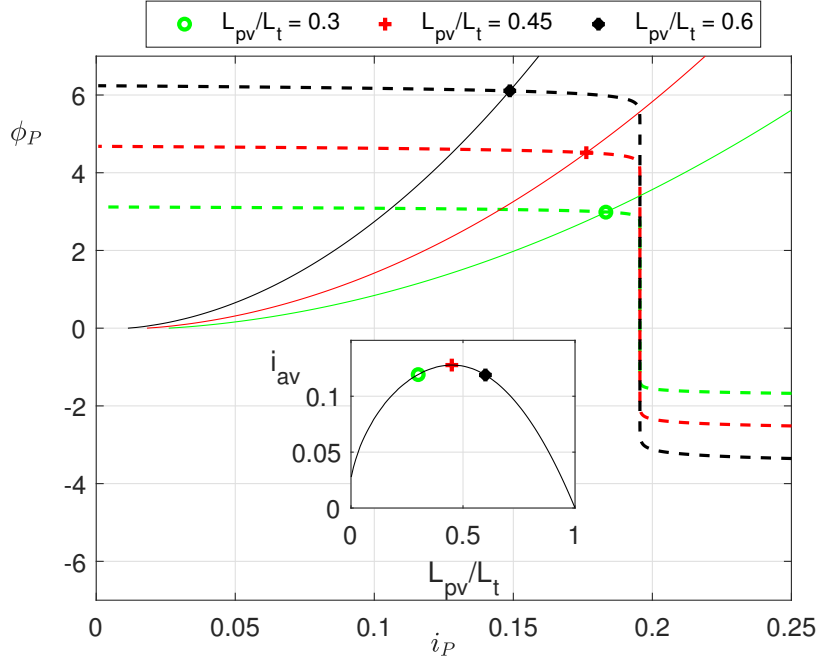


Figure 8: Design diagram for a bare-pv tether with an ideal electron emitter ( $V_C = 0$ ),  $\xi_t = 0.2$  and three values of  $L_{pv}/L_t$ . The inset shows  $i_{av}$  versus  $L_{pv}/L_t$ .

(a) and (c), for a very short bare segment, the bare tether has no current because the bias induced by the motional electric field is not high enough to overcome the potential drop of the electron emitter. We remind that we are assuming that the emitter emits no (any) current if the voltage is above (below)  $V_C < 0$ . Beyond a certain tether length,  $i_{av}$  and  $i_P$  increase monotonically (see Fig. 9).

A bare-pv tether behaves differently. For low  $L_b/L_*$ , even when a pure bare tether does not produce any current, the bare-pv tether has around  $i_{av} \approx 0.15$  thanks to the power delivered by the cells. As shown in panels (b) and (d), the voltage at the cells is close to the open-circuit voltage and the efficiency increases with the length of the bare segment, until reaching its maximum for  $L_b/L_* \approx 0.25$ . However, as  $L_b/L_*$  is increased, the condition  $i_P = i_{sc}$  is met at a certain point, i.e. the current collected by the bare segment is equal to the photocurrent (short-circuit current) of the cells ( $I_{sc}$ ). For this reason, there is a range

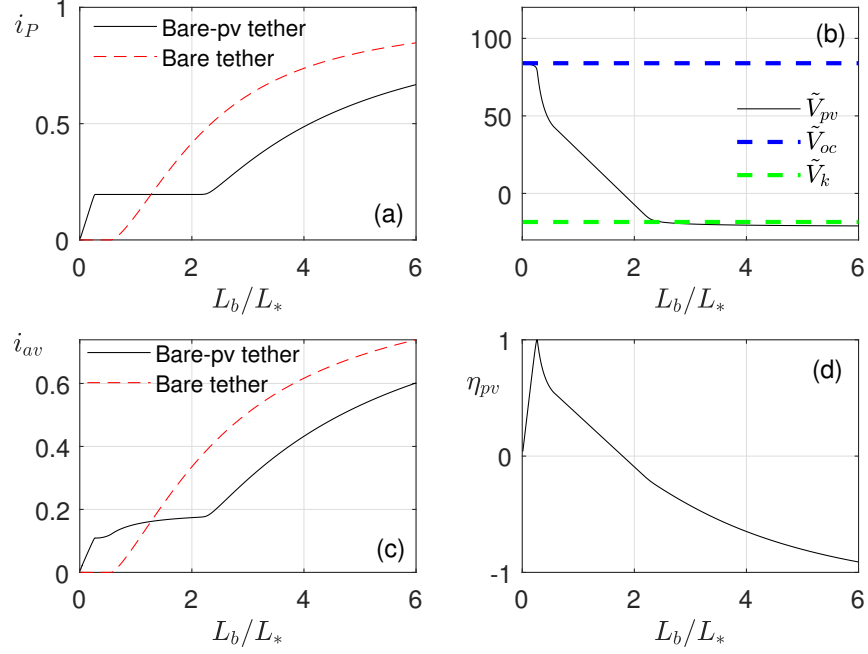


Figure 9: Performance of a bare-pv tether with the parameters of Table 1 and 2 versus the ratio  $L_b/L_*$ . Panels (a) to (d) show the normalized current at point P ( $i_P$ ), voltage of the cells  $\tilde{V}_{pv}$ , average current ( $i_{av}$ ), and the ratio  $\eta_{pv} = w_{pv}/w_{MPP}$ , respectively.

of  $L_b/L_*$  where  $i_P$  is constant and  $i_{av}$  increases weakly. As shown in panels (b) and (d), the bias at the cells and the efficiency decrease in that regime. For even higher values of  $L_b/L_*$ , the biases at the cells are negative enough to activate the bypass diode and allow the circulation of higher values of electric current. Both  $i_P$  and  $i_{av}$  increase with  $L_b/L_*$  as a pure bare tether but the performance are lower due to the potential drop at the bypass diodes. The pv segment wastes power and  $\eta_{pv}$  is negative in that regime.

### 4.3 High potential drop at the electron emitter

The design of a compact, autonomous, and consumable-less device based on a bare-pv tether for deorbiting a spacecraft is now studied. We will use the values of Tables 1 and 2, together with  $V_C = -1kV$  and  $f = 2$ . We consider three different values for the total tether

length ( $L_t \approx 340, 500$  and  $845$  m), which corresponds to  $\xi_t = 0.2, 0.3$  and  $0.5$ . Additionally, instead of fixing the length of the pv-segment as done before, the ratio  $L_{pv}/L_t$  is varied from zero (fully bare tether) to one (tether completely made of solar cells). Panels (a)-(d) in Fig. 10 show  $i_P$ , the anodic fraction of the bare tether length ( $L_{AB}/L_b$ ), and the two performance indexes  $i_{av}$  and  $\eta_{pv}$ . We first note that, for each value of  $\xi_t$ , there is a minimum of the ratio  $L_{pv}/L_t$  to make a current flow. If the length of the pv segment is too short, the bias induced by the motional electric field and the cells is not enough to reach the -1kV that is necessary to trigger the electron emission. As shown in panel (b), most of the bare tether has a negative bias for  $L_{pv}/L_t$  slightly higher than such a minimum and, as  $L_{pv}/L_t$  increases, the ratio  $L_{AB}/L_b$  quickly approaches to 1 (the complete bare segment is anodic).

Panels (c) and (d) reveal that, given a total tether length and if the system is well-designed, there is an optimum of  $L_{pv}/L_t$  that maximizes  $i_{av}$  and  $\eta_{pv}$  (see curves for  $\xi_t = 0.2$  and  $\xi_t = 0.3$ ). The maxima for  $i_{av}$  and  $\eta_{pv}$  occur for different (but close) values of  $L_{pv}/L_t$  and, the shorter the tether, the higher the optimal length of the pv segment. If the system is not well-designed, the photogenerated current acts as a bottleneck (see curve for  $\xi_t = 0.5$ ). Since  $i_{sc}$  is proportional to the cell area, it would be convenient in the  $\xi_t = 0.5$  case to increase the length of the cell size ( $L_{cell}$ ).

In order to find some definite numbers, let us focus on the optimum for the case  $\xi_t = 0.3$  that is reached for  $L_{pv}/L_t = 0.63$ . We then have  $L_t = 507m$ ,  $L_{pv} = 320m$ ,  $L_b = 187m$ , and the number of cells  $N_{cell} = 1546$ . The average current and the current at the cathode are  $I_* i_{av} \approx 0.35A$  and  $I_C = 0.42A$ , respectively. The mechanical power dissipated by the Lorentz force is

$$\mathbf{v} \cdot \mathbf{F}_L = -E_m \int_0^{L_t} I(x) dx = -\sigma_t E_m^2 A_t L_t i_{av} = -17.6W, \quad (35)$$

where we used Eq. (5) and  $\mathbf{v} \cdot (\mathbf{u}_t \times \mathbf{B}) = -E_m$ . These numbers fit well with Carbon-Nanotube (CNT) field-emission electron emitters, which do not require any heater power

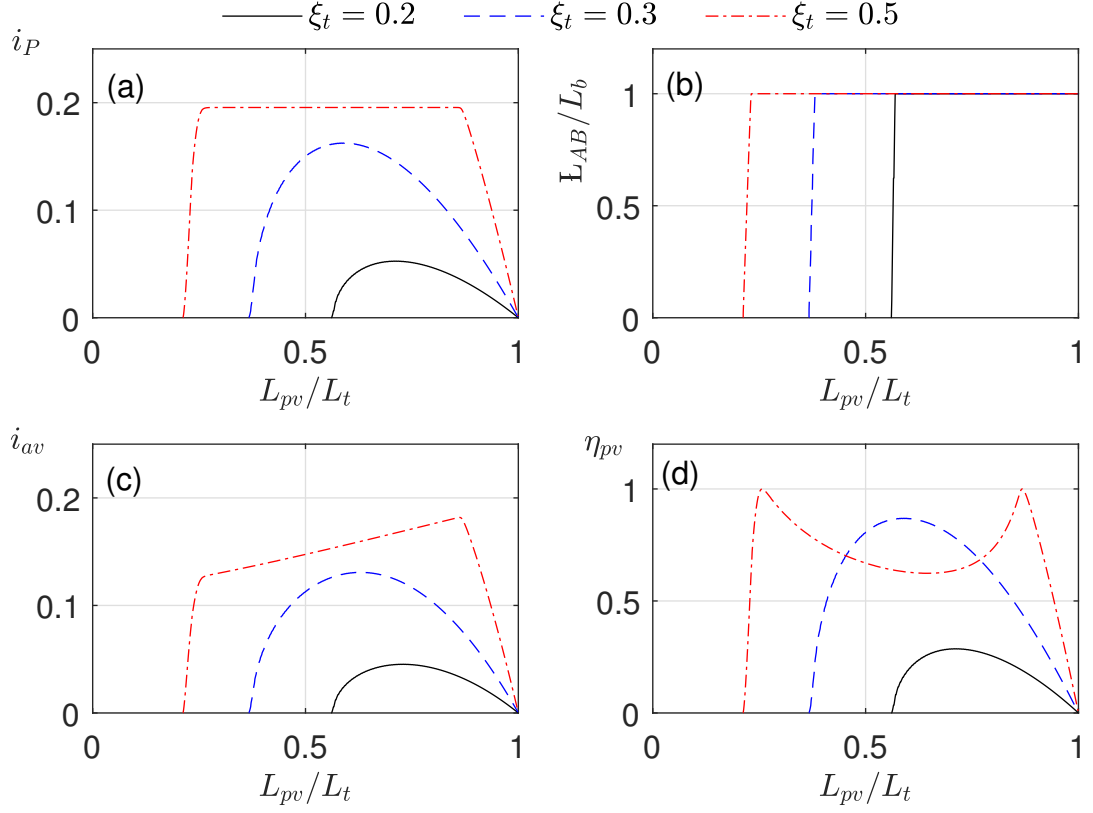


Figure 10: Effect of the ratio  $L_{pv}/L_t$  on tether performance.

and can be directly operated from the  $-1kV$  and current from the tether. Moreover, the current is distributed over such a large area that they do not run into space charge limitations when injected into the ambient plasma at higher altitudes. CNT electron emitters are currently being developed at TU Dresden for space applications and have already operated successfully in space [29]. Within the framework of the E.T.PACK project [17], similar CNT emitters are currently being scaled up to provide currents close to what we need for our estimate. Based on the development of the E.T.PACK project, a specific area of  $1,000cm^2/A$  and a specific mass of  $2.5kg/A$  are estimated. Considering the required current of  $I_C = 0.42A$ , this leads to a surface area of  $\approx 20 \times 20cm^2$  and a total mass of the

CNT emitter of  $m_{CNT} = 1kg$ , which seems realistic to be implemented on one side of the deorbit kit. Taking aluminum density for the bare segment ( $\rho_b = 2700kg/m^3$ ) and GaAs for the pv-segment ( $\rho_{pv} = 5300kg/m^3$ ), the total mass of the tether is  $m_t = (0.38 + 1.27)kg = 1.65kg$ .

## 5 Discussion

### 5.1 Design considerations

The results of Sec. 4 highlights the importance of making a correct design of the three elements of the tether system (bare segment, pv segment, and electron emitter). As shown in panels (a) and (c) of Fig. 9, a bare-pv tether can beat a bare tether, but only if designed correctly. The tether dimensions and the characteristics of the cells should be selected to make the pv segment operate close to the MPP. The cells should be sized to ensure that the current collected by the bare segment is lower than the photogenerated current. According to Eq. (27), and given a tether width and length of the pv segment, making the cells shorter can be positive because it will increase  $N_{cell}$  and the value of  $\phi_P$  (note that  $V_{pv} > V_k$  for a well-designed system). However, since the photogenerated current is proportional to the area of the cell, there is obviously an optimum in the cell size that should be studied carefully. Such analysis is beyond the scope of this work.

Equation (35) points out that, for a conventional bare tether, the mechanical power is proportional to  $E_m^2$ , i.e. the motional electric field appears twice in the analysis. First, due to the factor  $\mathbf{v} \cdot (\mathbf{u}_t \times \mathbf{B})$  and, secondly, because the current is below the tether short circuit current ( $I_* = \sigma_t A_t E_m$ ) and we have  $i_{av} < 1$ . This is an important feature because, since the variation of the spacecraft altitude with time scales as  $dh/dt \propto E_m^2$ , the deorbit time is typically proportional to  $E_m^{-2}$ . For high inclined orbits, where  $E_m$  is small if the tether is aligned with the local vertical, tether performance can be poor. However, the situation is different and more favorable for a bare-pv tether. The factor  $\mathbf{v} \cdot (\mathbf{u}_t \times \mathbf{B})$  remains, but

the system can be designed to reach  $i_{av} > 1$ . In addition to the natural motional electric field  $E_m$ , which is typically around 0.1 V/m, the cell contributes with an electric field of the order  $V_{oc}/L_{cell}$  that is much higher (around  $2.7V/0.207m \approx 13V/m$  in the example above). Besides enhancing tether performance, it also make the behavior of the tether less dependent on orbital parameters. As compared to a standard bare tether, a bare-pv tether can present much better performance in the congested Sun-synchronous orbits, where  $E_m$  is low but the illumination conditions are favorable.

## 5.2 Model adaptations for other modes and tether types

The schemes in panels (a) and (b) of Fig. 1 for bare-pv tethers can also be used to produce onboard power. For instance, in the case of panel (a), any useful load of impedance  $R$  interposed between the pv segment and the cathode will be fed by the tether. The electrical model remains the same, except that it is necessary to introduce the potential drop  $RI_P$  across the load. On the other hand, the modeling of a bare-pv tether in active mode (reboost in LEO) can be handled with the techniques used here. The main difference is that one has  $\mathbf{E} \cdot \mathbf{u}_t < 0$  and the right hand side of Eq. (9) reads  $i + 1$ . Besides a bare-pv tether, the analysis can also be applied to the operation of a fully bare tether in passive mode and with available power in the mother spacecraft. If available, it is convenient to connect the power source between the cathode and the bare tether. As shown in this work, the power injected in the tether-plasma circuit enhance tether performance and it can even generate tether current above the short circuit current  $I_*$ .

Previous discussion was mainly focused on a tether equipped with an active electron emitter. However, in case a low-W coating will be available, the current and voltage profiles along the LWT shown in panel (b) of Fig. 1 could be computed with a similar analysis. Assuming that the tether-to-plasma bias is negative enough in the coated segment (no space charge effects), the current at points S is

$$\frac{dI}{dx} = -p_t (j_{th} + j_{ph}) \rightarrow I_S = p_t L_c (j_{th} + j_{ph}), \quad (36)$$

where we used that  $I_C = 0$  for a LWT and the thermionic ( $j_{th}$ ) and photocurrent ( $j_{ph}$ ) current densities are constant throughout the coated segment. Explicit models for  $j_{th}$  and  $j_{ph}$  are given in Ref. [6], and they basically involve the properties of the coating like work function and photoelectric yield. Since we have  $I_S = I_P$ , Eq. (36) can be combined with the analysis of Secs. 3.1 and 3.2 to find  $I(x)$  and  $V(x)$ . An important aspect of the design of a bare-pv-coated tether is that, given the properties of the coating, the length of the coated segment  $L_c$  should be selected properly to match  $I_S$  with the optimal value required by the bare and the pv segments.

## 6 Conclusions

This work shows that an appropriate combination of a bare segment and a photovoltaic (pv) segment made of thin film solar cells can be a practical solution to develop a compact, autonomous, and consumable-less tether system. If designed correctly, the pv segment induces a strong negative bias at the cathode and opens the possibility to use consumable-less cathodic contactors like thermionic emitters and electron field emitter without the need of external power. This combination of bare and pv segments impacts positively on tether performance in both active and passive modes. In case a low-W coating will be available, the LWT concept can also benefit from the insertion of a pv portion between the bare and the coated segments. The analysis highlighted an important difference with respect to a standard bare tether in passive mode; thanks to the power delivered by the cells, the current in the bare segment can be larger than the tether short circuit current  $I_*$ . Consequently, the pv segment can enhance tether performance. In a practical application like spacecraft deorbiting, it means shorter deorbit time for the same tether length or shorter tether length for the same deorbit time. The proposed design scheme condense the full analysis in two figures that, if superimposed, allow to find straightforwardly the operation point of the system (currents and voltages).

The study shows that, in order to achieve optimal performance, it is necessary to



design the tether system carefully according to the inputs of the selected mission. The pv segment can certainly improve the performance, but it can also yield lower efficiencies than a pure bare tether if designed incorrectly. In particular, it is crucial to select the size of the cell to reach a high enough photogenerated current. Otherwise, the pv-segment acts as a bottleneck and an important potential drop is produced due to the bypass diodes of the cells. Since the performance of the bare tether depends on ambient conditions, including motional electric field and plasma density, some margins have to be considered to accomplish the constraints along the full mission. An example is the lack of delivered power by the pv segment during eclipses. Nevertheless, one of the most interesting characteristics of the system is its scalability. Given a mission, for instance the mass of the spacecraft to be deorbited and the characteristics of the initial orbit, the design parameters, including the dimensions of each of the tether segments, can be selected to reach high performance. The concept introduced in this work indicates that a fully autonomous and consumable-less tether system with high currents can be achieved using state-of-the-art components.

## Acknowledgments

This work received funding from the European Union’s Horizon 2020 research and innovation programme under grant agreement No 828902 (E.T.PACK project). GSA work is supported by the Ministerio de Ciencia, Innovación y Universidades of Spain under the Grant RYC-2014-15357.

## References

- [1] S. D. Drell, H. M. Foley, and M. A. Ruderman. Drag and propulsion of large satellites in the ionosphere: An alfvén propulsion engine in space. *Journal of Geophysical Research*, 70(13):3131–3145, 1965. doi: 10.1029/JZ070i013p03131.

- [2] R. Moore. The geomagnetic thruster - a high performance "alfven wave" propulsion system utilizing plasma contacts. pages AIAA paper No. 66-257, 1966. doi: 10.2514/6.1966-257.
- [3] M. Grossi. Future of Tethers in Space. *Proceedings of Fourth International Conference on Tethers in Space, Science and Technology*, pages 11-23, 1995.
- [4] J. R. Sanmartin, M. Martinez-Sanchez, and E. Ahedo. Bare Wire Anodes for Electrodynamic Tethers. *Journal of Propulsion Power*, 9:353-360, 1993. doi: 10.2514/3.23629.
- [5] J. D. Williams, J. R. Sanmartín, and L. P. Rand. Low Work-Function Coating for an Entirely Propellantless Bare Electrodynamic Tether. *IEEE Transactions on Plasma Science*, 40:1441-1445, May 2012. doi: 10.1109/TPS.2012.2189589.
- [6] G. Sanchez-Arriaga and Xin Chen. Modeling and Performance of Electrodynamic Low-Work-Function Tethers with Photoemission Effects. *Journal of Propulsion and Power*, 34(1):213-220, JAN 2018. doi: 10.2514/1.B36561.
- [7] J. Pelaez, E.C. Lorenzini, O. Lopez-Rebollal, and M. Ruiz. A new kind of dynamic instability in electrodynamic tethers. *Journal of the Astronautical Sciences*, 48(4):449-476, Oct-Dec 2000. AAS/AIAA 10th Space Flight Mechanics Meeting, Clearwater, Florida, Jan 23-26, 2000.
- [8] ELM Lanoix, AK Misra, VJ Modi, and G Tyc. Effect of electrodynamic forces on the orbital dynamics of tethered satellites. *Journal of Guidance Control and Dynamics*, 28(6):1309-1315, Nov-Dec 2005. doi: 10.2514/1.1759.
- [9] Y Yamaigiwa, E Hiragi, and T Kishimoto. Dynamic behavior of electrodynamic tether deorbit system on elliptical orbit and its control by Lorentz force. *Aerospace Science and Technology*, 9(4):366-373, JUN 2005. doi: 10.1016/j.ast.2004.09.005.

- [10] Gangqiang Li, Zheng H. Zhu, and S. A. Meguid. Libration and transverse dynamic stability control of flexible bare electrodynamic tether systems in satellite deorbit. *Aerospace Science and Technology*, 49:112–129, FEB 2016. doi: 10.1016/j.ast.2015.11.036.
- [11] R. Mantellato, L. Olivieri, and E.C. Lorenzini. Study of dynamical stability of tethered systems during space tug maneuvers. *Acta Astronautica*, 138:559 – 569, 2017. doi: 10.1016/j.actaastro.2016.12.011.
- [12] J. R. Sanmartin, A. Sanchez-Torres, S. B. Khan, G. Sanchez-Arriaga, and M Charro. Optimum Sizing of Bare-Tape Tethers for De-Orbiting Satellites at end of Mission. *Advances in Space Research*, 56:1485–1492, 10 2015. doi: 10.1016/j.asr.2015.06.030.
- [13] S. B. Khan and J. R. Sanmartin. Survival Probability of Round and Tape Tethers Against Debris Impact. *Journal of Spacecraft and Rockets*, 50:603–608, May 2013. doi: 10.2514/1.A32383.
- [14] Shaker Bayajid Khan, A. Francesconi, C. Giacomuzzo, and E. C. Lorenzini. Survivability to orbital debris of tape tethers for end-of-life spacecraft de-orbiting. *Aerospace Science and Technology*, 52:167–172, MAY 2016. doi: 10.1016/j.ast.2016.02.033.
- [15] Ricardo Garcia-Pelayo, Shaker Bayajid Khan, and Juan R. Sanmartin. Survivability analysis of tape-tether against two concurring impacts with debris. *Advances in Space Research*, 57(11):2273–2284, JUN 1 2016. doi: 10.1016/j.asr.2016.03.018.
- [16] Carmen Pardini, Toshiya Hanada, and Paula H. Krisko. Benefits and risks of using electrodynamic tethers to de-orbit spacecraft. *Acta Astronautica*, 64(5-6):571–588, Mar-Apr 2009. doi: 10.1016/j.actaastro.2008.10.007.
- [17] G. Sánchez-Arriaga, S. Naghdi, K. Waetzig, J. Schilm, E.C. Lorenzini, M. Tajmar, E. Ugoiti, L. Tarabini Castellani, J.F. Plaza, and A. Post. The e.t.pack project:

- Towards a fully passive and consumable-less deorbit kit based on low-work-function tether technology. *Acta Astronautica*, 2020. doi: 10.1016/j.actaastro.2020.03.036.
- [18] Dan R. Lev, Ioannis G. Mikellides, Daniela Pedrini, Dan M. Goebel, Benjamin A. Jorns, and Michael S. McDonald. Recent progress in research and development of hollow cathodes for electric propulsion. *Reviews of Modern Plasma Physics*, 3(1):6, Jun 2019. doi: 10.1007/s41614-019-0026-0.
- [19] RL Forward, RP Hoyt, and CW Uphoff. Terminator Tether (TM): A spacecraft deorbit device. *Journal of Spacecraft and Rockets*, 37(2):187–196, MAR-APR 2000. doi: 10.2514/2.3565.
- [20] J. R. Sanmartin, R. D. Estes, E. C. Lorenzini, and S. A. Elaskar. Efficiency of electrodynamic tether thrusters. *Journal of Spacecraft and Rockets*, 43(3):659–666, May 2006. doi: 10.2514/1.16174.
- [21] Jinyu Liu, Gangqiang Li, Zheng H. Zhu, Ming Liu, and Xingqun Zhan. Automatic orbital maneuver for mega-constellations maintenance with electrodynamic tethers. *Aerospace Science and Technology*, 105:105910, 2020. doi: 10.1016/j.ast.2020.105910.
- [22] Iverson C. Bell, Brian E. Gilchrist, Jesse K. McTernan, and Sven G. Bilen. Investigating Miniaturized Electrodynamic Tethers for Picosatellites and Femtosatellites. *Journal of Spacecraft and Rockets*, 54(1):55–66, JAN 2017. doi: 10.2514/1.A33629.
- [23] AZUR SPACE Solar Power GmbH. 30% Triple Junction GaAs Solar Cell. *www.azurspace.com*, Issue Date 2016-08-19. *www.azurspace.com*.
- [24] A. Luque and S. Hegedus. *Handbook of Photovoltaic Science and Engineering*. Wiley, 2003.

- [25] M. Sanjurjo, G. Sanchez-Arriaga, and J. Pelaez. Efficient computation of current collection in bare electrodynamic tethers in and beyond oml regime. *Journal of Aerospace Engineering*, 0:04014144, 2014. doi: 10.1061/(ASCE)AS.1943-5525.0000479.
- [26] J. R. Sanmartín and R. D. Estes. The Orbital-Motion-Limited Regime of Cylindrical Langmuir Probes. *Physics of Plasmas*, 6:395–405, January 1999. doi: 10.1063/1.873293.
- [27] J. G. Laframboise. *Theory of Spherical and Cylindrical Langmuir Probes in a Collisionless, Maxwellian Plasma at Rest*. PhD thesis, University of Toronto (Canada)., 1966.
- [28] G. Sánchez-Arriaga, C. Bombardelli, and X. Chen. Impact of Nonideal Effects on Bare Electrodynamic Tether Performance. *Journal of Propulsion and Power*, 31(3):951–955, 2015. doi: 10.2514/1.B35393.
- [29] P. Laufer and M. Tajmar. Cnt-based cold electron source for space applications on nanosatellites. September 15-20, Vienna, Austria, 2019. 36th International Electric Propulsion Conference (IEPC).